We are IntechOpen,
the world's leading publisher of Open Access books
Built by scientists, for scientists

6,900
Open access books available

185,000
International authors and editors

200M
Downloads

154
Countries delivered to

Our authors are among the

TOP 1%
most cited scientists

12.2%
Contributors from top 500 universities

BOOK CITATION INDEX
CLARIVATE ANALYTICS
INDEXED

WEB OF SCIENCE™

Selection of our books indexed in the Book Citation Index
in Web of Science™ Core Collection (BKCI)

Interested in publishing with us?
Contact book.department@intechopen.com

Numbers displayed above are based on latest data collected.
For more information visit www.intechopen.com

Time-Spectral Visualization of Fundamental Ultrafast Nonlinear-Optical Interactions in Photonic Fibers

Anatoly Efimov
Center for Integrated Nanotechnologies, Los Alamos National Laboratory
USA

1. Introduction

Recent renewed interest to nonlinear optical processes in waveguiding structures was sparked in large part by the original reports on broadband supercontinuum (SC) generation in photonic crystal fibers (PCF) and uniform fiber tapers (Ranka et al., 2000; Birks et al., 2000) introduced a few years earlier by the group in Bath (Knight et al., 1996; Knight, 2003). The significance of these first reports stemmed from the fact that it was sufficient to use femtosecond oscillators only (nanojoule pulse energies) to produce octave-spanning continua in the visible. The fact that the broadband spectra emitted from a PCF pumped with femtosecond pulses centered at 800 nm covered all of the visible range and thus were easily observed with the naked eye as a spectacular rainbow of colors must have had something to do with the subsequent popularity of this research area. This is because in the previous decade and even much earlier a number of works reported broadband continuum generation in the near-infrared (Lin et al., 1978; Morioka et al., 1994), which remained unnoticed by the wider optics community. Those older studies were usually performed with pump sources at 1550 nm and were targeted towards telecom applications at that time. Subsequent studies unveiled important differences in SC generation mechanisms and their properties depending on the fiber or PCF parameters and the duration of the pump pulse. One very important advantage of a SC generated with femtosecond pulses is its high degree of coherence over the whole or most of the generated spectrum (Dudley et al., 2006), making it useful for a number of advanced applications, such as absolute phase stabilization of ultrashort pulses (Jones et al., 2000) and frequency metrology (Udem et al., 2002).

Importantly, it was soon realized that PCFs and other engineered structures allow for much greater flexibility in dispersion design, in addition to high effective nonlinearities due to strong confinement of the transverse optical mode. In large part it was the particular shape of the dispersion profile of the PCF as a function of the wavelength, which fortuitously allowed for broadband SC generation in the early experiments. The importance of dispersion should not be underestimated as it controls various phasematching conditions for nonlinear optical processes, such as emission of Cherenkov continuum (responsible for the visual portion of the typical SC) by solitons (Wai et al., 1990; Karpman, 1993; Akhmediev & Karlsson, 1995). Solitons themselves play an important role in the process of SC generation and thus must be studied carefully. However, spectroscopic measurements are

not sufficient in many situations to uncover the fundamental physics involved. The same example of SC generation clearly demonstrates this: By looking at the spectrum recorded at the output of a long PCF it is virtually impossible to extract any useful information on the underlying dynamical mechanisms in play behind its generation, even though the excitation pulse had a well-defined temporal structure, usually a transform-limited pulse of a few tens of femtoseconds in duration.

Temporal resolution in the measurements, thus appears as important as spectral one and a number of time-resolved techniques exist, which are applicable to waveguiding geometries. Importantly, however, any linear interferometric method, such as spectral interferometry, can not be applied to the highly nonlinear propagation regimes of interest, because the output spectrum differs significantly from the input one. Thus, nonlinear methods (featuring ultrafast nonlinear gating) must be used. Two encompassing domains can be identified: auto-correlation and cross-correlation methods. The autocorrelation approaches are very well suited for the characterization of unknown pulses, e.g. the output pulse from a femtosecond laser (Trebino, 2000). Here, the unknown pulse gates itself, so to speak, to produce a nonlinear autocorrelation trace of a specific shape, depending on the particular nonlinear mechanism used, which carries information about the amplitude and the phase of the unknown pulse, which can be extracted. Often times some fundamental limitations apply, such as time-reversal symmetry for second harmonic generation (SHG) frequency-resolved optical gating (FROG). In addition, technical difficulties arise if complex or broadband pulses are being measured, such as phasematching bandwidth requirements for SHG FROG or spectral phase interferometry for direct electric field reconstruction (SPIDER), or sensitivity in polarization-gating FROG and others. This is why the very first time-resolved images of supercontinuum generated in silica PCFs were obtained using cross-correlation methods—the sum-frequency generation (SFG) X-FROG (Dudley et al., 2002) and cross-correlation sonogram measurements (Hori et al., 2004). In a typical cross-correlation approach the signal pulse is gated with a different reference pulse, usually a replica of the input pump pulse split off before the nonlinear medium under study and appropriately delayed. While sonogram measurements require both delay and spectral filter scanning to obtain the 2D time-frequency image of the pulse (Taira & Kikuchi, 2001), the SFG X-FROG approach requires only one delay scan with wavelength resolution achieved by spectrally resolving the upconverted sum-frequency signal, and thus is simpler to implement with off the shelf components.

For our intended work on visualizing weak and broadband signals the optimal measurement technique must be sensitive and broadband itself, as well as yield the most intuitive images of the output pulse possible. Arguably, the SFG X-FROG fits the bill very well. In this second-order nonlinear cross-correlation type measurement technique a portion of the pulse from the laser is used to gate the signal pulse. The total two-dimensional spectrogram is built by scanning the delay between the signal and reference pulses and acquiring the spectrum of the SFG signal (Linden et al., 1998):

$$I_{X-FROG}^{SFG}(\omega,\tau) = \left| \int_{-\infty}^{+\infty} E_{sig}(t) \, E_{ref}(t-\tau) \, e^{-i\omega t} dt \right|^2 , \tag{1}$$

where $I_{X-FROG}^{SFG}(\omega,\tau)$ is the intensity of the X-FROG signal as a function of optical frequency ω and delay τ produced by cross-correlating the signal $E_{sig}(t)$ with the delayed reference

$E_{ref}(t-\tau)$ electric field pulses. Expression (1) is written specifically for sum-frequency $\omega_{SF} = \omega_{sig} + \omega_{ref}$ generation X-FROG where the product of two fields is obtained through SFG in a thin crystal with instantaneous quadratic nonlinearity and the Fourier transform is obtained using a spectrometer. The focal plane detector of the spectrometer measures the spectral intensity, hence the spectrogram is proportional to the modulus squared of the spectrum of the sum-frequency generated signal. Special reconstruction algorithms can be used to recover the complete temporal behavior of the electric field, or equivalently, the amplitude and the phase of the optical pulse in either temporal or spectral domains. Most importantly, however, the information conveyed by the 2D X-FROG spectrogram itself allows one to grasp the whole picture of a complex ultrashort pulse visually. The fact that a spectrogram may be a much better representation of a complex pulse, than a pair of phase and amplitude curves in either time or spectral domains, was recognized by Treacy back in 1971 (Treacy, 1971). Moreover, highly intuitive nature of the (nearly) constrain-free X-FROG spectrograms is becoming increasingly attractive for theorists as well, who often find it to be the most suitable way to represent data from numerical simulations (Hilligsøe et al., 2004; Skryabin & Yulin, 2005). This fact facilitates direct visual comparison between theory and experiment, as is shown below.

X-FROG can be used to study a wide variety of propagation effects ranging from well-established processes to novel nonlinear regimes with ultrashort optical pulses, continuous waves (!) and their interactions. In what follows, our X-FROG setup developed for experimental work at telecom wavelength with arbitrary fibers is briefly described first (Efimov & Taylor, 2005a). Several illustrative examples of soliton formation in 100 meters of regular fiber and Raman soliton dynamics in standard cobweb PCFs (Efimov & Taylor, 2005b) are presented next, followed by more interesting cases of Cherenkov continuum generation by stabilized solitons in the vicinity of a second zero-dispersion (2ZD) point of a small-core PCF (Efimov et al., 2004). Resonant interactions of solitons and dispersive waves (Efimov et al., 2005c; Efimov et al., 2006) are illustrated next where excellent agreement with theoretical predictions was obtained. Further, experimental measurements and numerical simulations of SC in highly-nonlinear soft glass SF6 PCF are compared, where again we find excellent agreement, except for the solitonic part of the trace, where temporal jitter of solitons smears the experimental picture, revealing the effect of subtle instabilities present at the output of the pump laser used in the experiment (Efimov & Taylor, 2008). Finally, recent results on soliton dynamics and continuum generation across the bandgaps of an all-glass photonic bandgap fiber (PBF) are summarized before concluding this chapter.

2. X-FROG system and simple visualization examples

Performing cross-correlation type measurements requires matching optical propagation path lengths for both the signal and the reference arms. This is easily done with mechanical delay stages for relatively short samples, up to a meter or so long. Longer fiber samples will require more clever approaches. One interesting solution was offered in (Nishizawa & Goto, 2001) where the reference pulse is derived from the part of the generated signal as the red-most soliton, filtered out by a long-pass filter. An adjustable delay line was still needed after the fiber sample to provide delay scanning. Hori, et al. built a completely electronically controlled delay scanning using a separate fiber in the reference arm of their cross-

correlation sonogram system, where an acousto-optic modulator was used to vary the input power launched in the reference fiber, thus adjusting the delay of the propagating Raman soliton (Hori et al., 2003). In this approach the delay variation is intimately connected with soliton's central frequency. Although certainly creative, these delay scanning tactics are somewhat complicated and not universally applicable to any experimental situation. Thus, in our system we used a simple free-air delay stage and relied on the fact that, aside from the carrier-envelope phase (which is not measured by X-FROG) all the pulses in a pulse train produced by the laser are identical and therefore different pulses can be used as signal and reference.

The X-FROG system designed for use with arbitrarily long fibers is shown in Fig. 1. An optical parametric oscillator (OPO) generates a train of 100 fs pulses tunable in the range 1400-1600 nm with repetition rate of 82 MHz and average power up to 350 mW. A polarizing beam splitter separates the signal and the reference pulses. The former is coupled into the fiber under study using an aspheric lens and the latter propagates in a free-space 4-meter delay stage, equipped with precision retroreflecting corner cubes. The delay line of the X-FROG system is designed to provide optical delays in excess of the time spacing between individual pulses in the pulse train, thus allowing cross-correlation of different pulses within the pulse train generated by the OPO. The jitter of pulse temporal positions within the pulse train does not influence the results even for 100 meter-long fibers. The reference and the signal pulses are subsequently mixed in a 200 μm thick BBO crystal to generate sum-frequency signal, which is spectrally resolved in a grating spectrometer. The phasematching bandwidth of the nonlinear crystal at this particular wavelength region is sufficient to accurately convert more than an octave of signal spectrum, due to favorable material dispersion in the crystal.

Phasematching bandwidth available for SFG is, in fact, one of the most critical parameters of the whole system. From the long history of autocorrelation measurements of ultrashort pulses it is known that sufficiently thin crystals are required since the phasematching bandwidth is inversely proportional to the length of the nonlinear medium (Weiner, 1983). Interestingly, chirped pulses may appear shorter if measured with thick nonlinear crystals. This is because the narrow phasematching bandwidth effectively cuts the wings of the
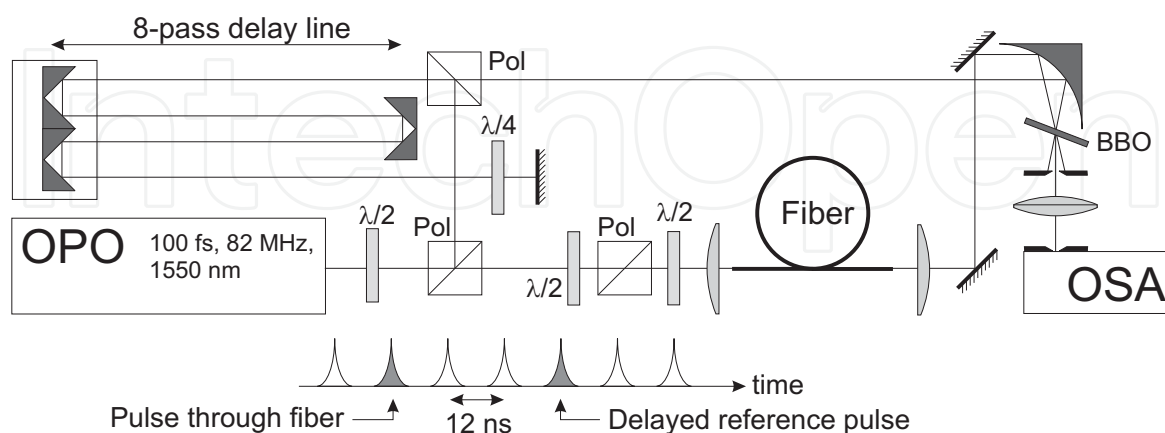

Fig. 1. SFG X-FROG system for studying pulse dynamics in fibers of arbitrary length. Schematically shown at the bottom is the pulse train generated by the laser system with separate reference and signal pulses shaded. Pol—polarizer, λ/2 and λ/4 are the waveplates.

pulse's spectrum, which for a chirped pulse, correspond to the leading and trailing edges of the pulse in time, making the autocorrelation trace appear shorter. For a uniaxial crystal, such as BBO, there are two phasematching possibilities for SHG: Type 1 $o + o \rightarrow e$, and Type 2 $o + e \rightarrow e$, where o and e denote "ordinary" and "extraordinary" rays respectively. For the SFG process, however, used in X-FROG there exist two distinct Type 2 processes: $o_{sig} + e_{ref} \rightarrow e_{SF}$ or $e_{sig} + o_{ref} \rightarrow e_{SF}$ because the signal and the reference are not identical. Using the "ordinary" and "extraordinary" refractive index data for the nonlinear crystal used in the system, all three cases may be examined for phasematching bandwidth, Fig. 2, and the most optimal configuration selected for the experiment. In Fig. 2 all three phasematching cases are represented for the reference wavelength of 1.55 μm and 200 μm thick BBO crystal. Clearly, more than an octave bandwidths are possible in all three cases. Most of the experiments described below were performed around the pump wavelength of 1.55 μm so the most optimal case for us is the Type 1 process, which also provides almost 2000 nanometers of bandwidth.
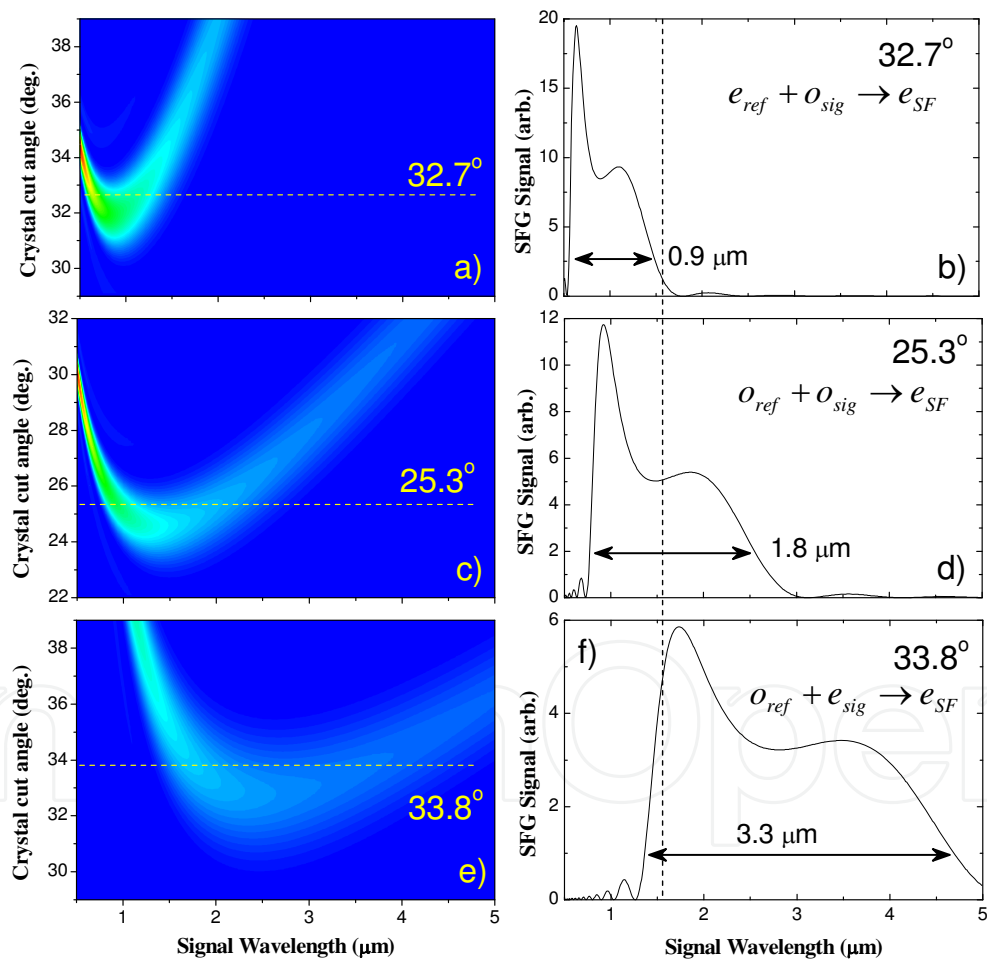

Fig. 2. Phase matching curves for non-collinear sum-frequency generation of a fixed wavelength reference pulse at 1.55 μm and variable wavelength signal pulse in a 200 μm BBO crystal. Left: density plots for crystal cut angle vs. signal wavelength. Dashed lines show most optimal cut angles for obtaining large phasematching bandwidths, and corresponding phasematching curves are plotted on the right for three possible arrangements. Vertical dashed line indicates λ = 1.55 μm central wavelength.
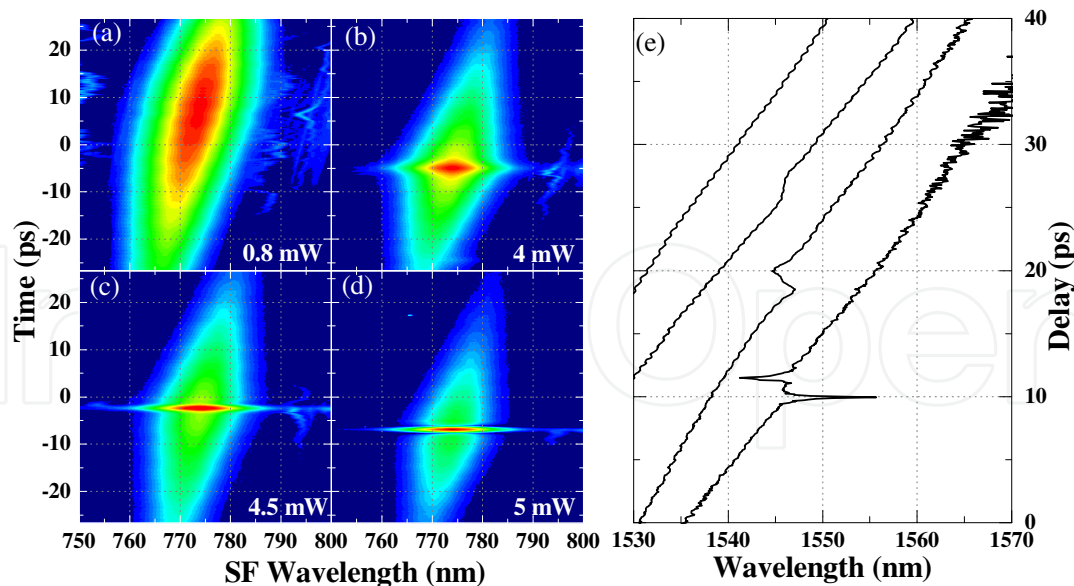
Fig. 3. X-FROG traces at the output of 100 meters of 3M FS-PM-7811 fiber. Average input power increases sequentially from (a) 0.8 mW, to (b) 4 mW, to (c) 4.5 mW to (d) 5 mW. Color scale mapping is logarithmic with the SFG signal intensity. (e) Wavelength-dependent group delay for several input powers obtained directly from respective X-FROG traces in (a-d). Curves are offset for clarity. Power increases from top to bottom.

As a simple demonstration of SFG X-FROG sensitivity and very intuitive traces produced, consider the problem of soliton formation in a regular single-mode fiber. Fig. 3 displays a series of traces taken at the output of a 100 meter-long piece of single-mode fiber (3M FS-PM-7811). Sensitivity of the system is sufficient to obtain more than 40 dB of signal-to-noise ratio even in the linear pulse propagation regime, Fig. 3a. As the input power is increased, soliton formation is observed with linear waves present on the wings, Fig. 3b-d. Naturally, blue (red) spectral components of the linear wave lead (trail) the soliton. As the input power is increased, a larger fraction of the input pulse energy contributes to the soliton.

It is interesting to observe the dynamics of the wavelength-dependent group delay as a function of the input power directly from the X-FROG trace, i.e. without applying reconstruction algorithms, as was suggested in (Treacy, 1971). The data shown in Fig. 3e is obtained by following the "center of mass" of each spectrum slice from the corresponding spectrogram in time. Each curve in the figure in sequence from top to bottom is obtained from the respective X-FROG trace from Fig. 3a-d. Formation of group delay features near the soliton position is clearly visible. Qualitatively, the behavior of the group delay versus wavelength is easy to understand when the soliton is almost formed: At the wings away from soliton the linear chirped wave gives rise to the wavelength-dependent delay due to dispersion in the fiber. The soliton, however, being a nonlinear wave maintains all its wavelength components at the same delay (no chirp) which corresponds to the near-horizontal section of the curve at the location of the soliton.

Soliton propagation at telecom wavelengths in a standard cobweb PCF presents another interesting example for visualization of the nonlinear dynamics. The fiber used for these experiments is a high-delta silica microstructured fiber with a 2.5 μm guiding core, 63 mm in length. Fig. 4 shows a series of X-FROG traces recorded at the output of the PCF for varying input powers of the pump pulse. The input wavelength is located well within the
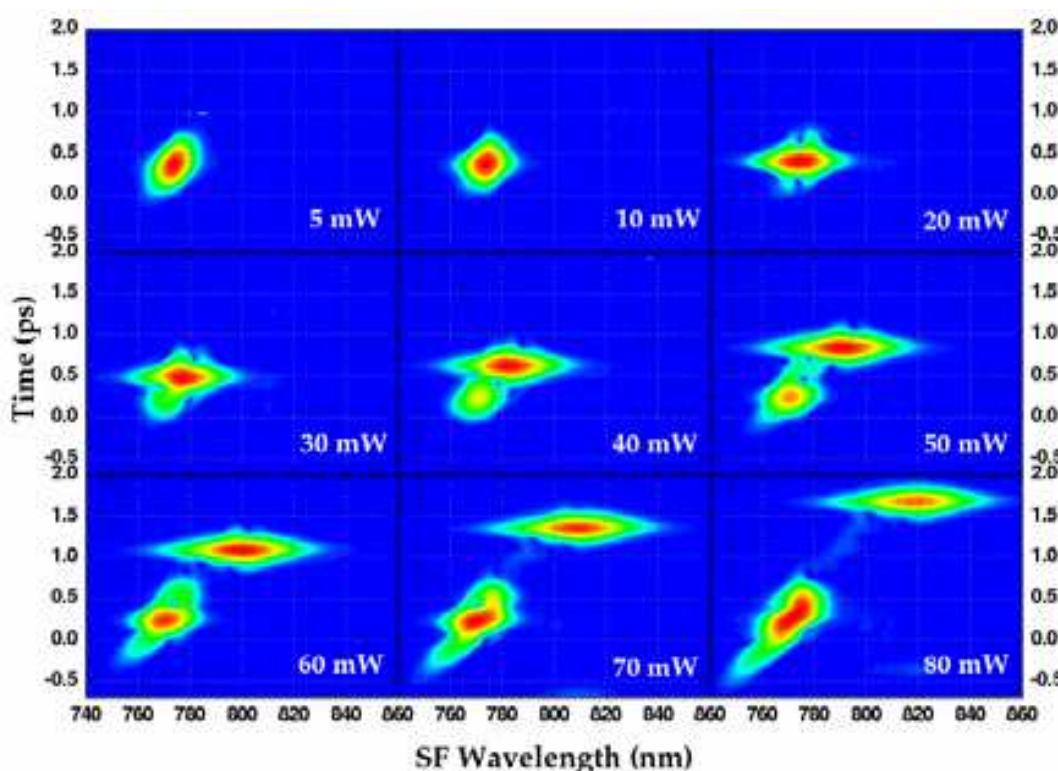
Fig. 4. Power-dependent X-FROG traces at the output of 2.5 μm-core cobweb PCF, 63 mm in length. Formation of a Raman-shifting soliton is clearly observed. Horizontal axis corresponds to sum-frequency signal wavelength. Color scale is logarithmic

anomalous dispersion region of this fiber so no broadband supercontinuum generation is observed. At high powers, however, intermodally phase-matched third harmonic generation occurs in which the Raman soliton dynamics plays crucial role (Efimov & Taylor, 2005b). At 5 mW the propagation of the fundamental pulse is nearly linear, which can be inferred from the elliptical shape of the trace as well as parabolic phase from X-FROG reconstruction, Fig. 5, in both temporal and spectral domains. Soliton formation sets in at about 10 mW average power, at which point the X-FROG trace assumes the required diamond-like shape, characteristic to the Sech(t) temporal amplitude profile. Spectral and temporal phase functions, Figs. 5a and 5b show substantial flattening, as expected, for 10 mW and 20 mW input powers. Using the parameters of this silica PCF (effective area $A_{eff} = 5 \mu m^2$, nonlinear index $n_2 = 3 \cdot 10^{-16} cm^2 W^{-1}$, dispersion $D = 200 ps \cdot nm^{-1} km^{-1}$) and input pulse duration of 100 fs we can estimate the average power, corresponding to the fundamental soliton, to be about 17 mW, which agrees well with the experiment if the fiber coupling efficiency of ~60% is taken into account.

With further increase of the input power pulse splitting and Raman self-frequency shift of the main soliton can be clearly seen. The frequency shifting soliton maintains the diamond-like X-FROG shape which is a clear evidence for the solitonic Sech(t) amplitude profile. From the reconstructed spectral phase functions we see that the Raman soliton remains flat-phased (the tilt of the phase function corresponds to linear shift on the time axis), whereas the pulse remaining in the vicinity of the pump wavelength is, in fact, chirped, as evidenced by the curved phase in Fig. 5b. The wavelength shift of the Raman soliton is accompanied by the delay offset in accordance with the anomalous dispersion of the fiber. With increasing
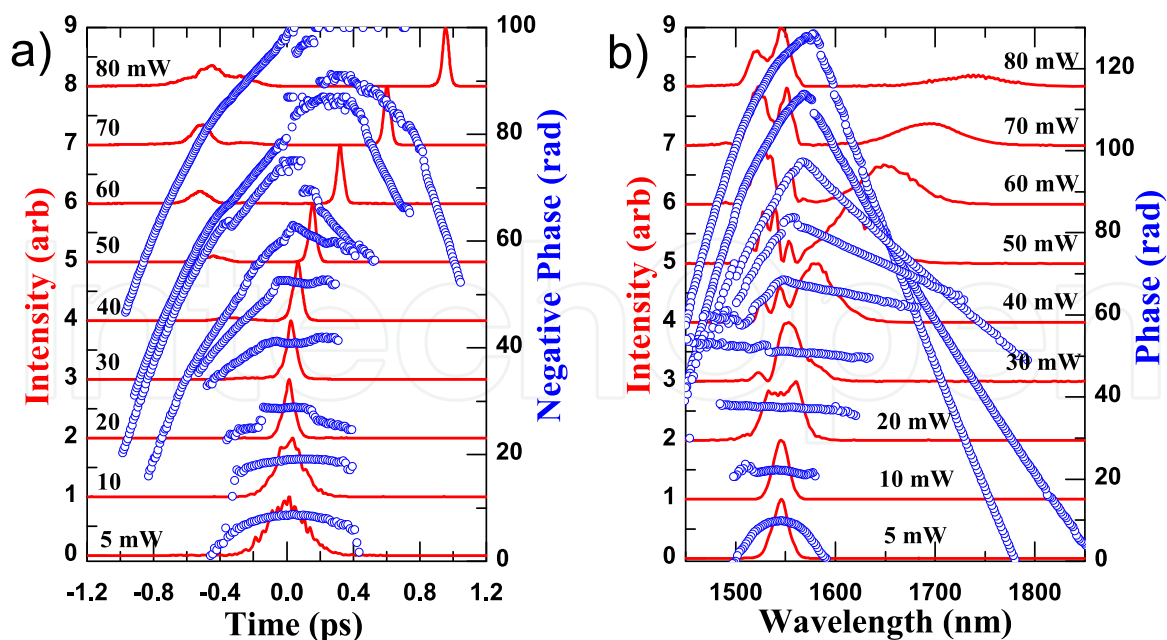
Fig. 5. Intensity (colid curves) and phase (circles) of the pulse in temporal, (a), and in spectral, (b), domains at the output of the PCF reconstructed from the experimental X-FROG spectrograms of Fig. 4. Reconstruction error does not exceed 0.002 on 256 × 256 grid for all power levels. Input power increases from bottom to top as indicated.

input power the spectral width of the Raman soliton increases and at the same time the temporal duration of the soliton reduces since the Raman soliton constitutes a transform-limited pulse. At the 80 mW input power the intensity full-width at half-maximum of the Raman soliton shrinks to 42 fs, which gives the soliton compression ratio of ~2.5 times.

3. Soliton dynamics near the second dispersion zero in a small-core PCF

Novel regimes of nonlinear soliton dynamics can be realized in strongly guiding waveguides. When the waveguide is designed for strong confinement of the mode, usually by using large index difference between the core and the cladding, the waveguide contribution to the total dispersion may become compatible and even exceed the material dispersion. For such waveguides with core diameters on the order of the wavelength a second zero dispersion (2ZD) point may exist at a longer wavelength. The dispersion slope $\dfrac{\partial D(\lambda)}{\partial \lambda}$ in the vicinity of the 2ZD point is negative, whereas it is positive near the first zero-dispersion point, typical for the regular fibers and previous generations of PCFs (Ranka et al., 2000; Dudley et al., 2002; Dudley et al., 2006). Theoretical predictions (Skryabin & Yulin, 2005; Biancalana et al., 2004) and previous experiments (Harbold et al., 2002; Skryabin et al., 2003; Genty et al., 2004) suggested unusual soliton dynamics in the vicinity of the 2ZD point. These effects may have far-reaching consequences since the wavelength of the 2ZD point can be tuned to the telecommunications region around 1550 nm through careful control of the fiber structure during manufacturing.

Figure 6 shows the dispersion and the optical loss for two of the fibers used in our experiments. The 2ZD points for two fibers shown are located at 1510 and 1560 nm and measured dispersion slopes are large and negative. The dispersion of a regular fiber is
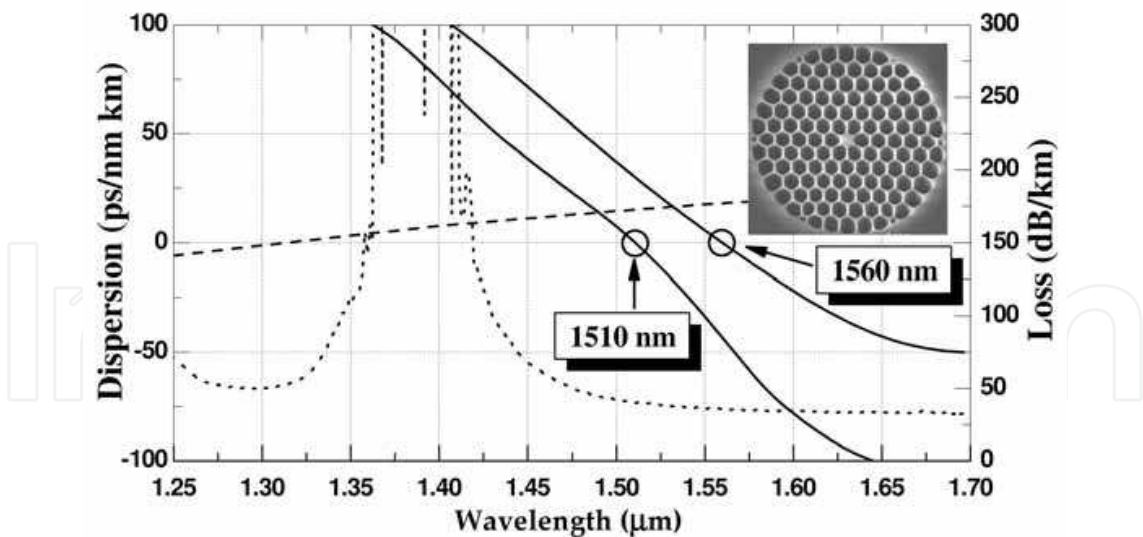
Fig. 6. Optical properties of small-core PCFs. Solid lines—dispersion curves for two distinct fibers; dotted curve—attenuation. For comparison the dispersion of a regular telecom fiber is shown with the dashed curve. Inset—scanning electron microscope image of one of the PCFs; the central guiding core diameter is about 1.2 µm.

shown for comparison in the figure with a dashed curve. The small core of the fiber also provides for high peak intensities for the propagating optical pulses. The nonlinear parameter for these PCFs is estimated to be $\gamma \sim 100 \cdot W^{-1}km^{-1}$, about two orders of magnitude larger than in standard telecom fibers. Note that in the vicinity of the 2ZD point, anomalous dispersion regime is realized at shorter wavelengths whereas normal dispersion lies at longer wavelengths. Thus, solitons launched on the anomalous dispersion side are pushed toward the 2ZD by the Raman effect, rather than away, as would be the case near the first ZD point. One interesting consequence of this fact is that the soliton gets stabilized near the 2ZD through spectral recoil while emitting the Cherenkov continuum across the 2ZD point at longer wavelengths (Skryabin et al., 2003) according to the phase-matching condition (Lu et al., 2005):

$$\Delta\beta \equiv \beta(\omega_s) - \beta(\omega_{cher}) + \frac{\omega_{cher} - \omega_s}{v_g} + \gamma P_s = 0 \, , \tag{2}$$

where β is the propagation constant, ω_s and ω_{cher} are the soliton and the Cherenkov continuum frequencies, respectively; v_g is the soliton's group velocity; γ is the fiber's nonlinear coefficient, and P_s is the soliton peak power. Since the soliton never crosses the 2ZD point, it is clear, also, that the soliton can potentially transfer all of its energy to the Cherenkov continuum (Chen et al., 2009).

Detailed time-spectral dynamics of a soliton propagating in the vicinity of 2ZD point of a small-core PCF, observed with X-FROG is shown in Fig. 7. The PCF is pumped in the anomalous dispersion region at 1440 nm (λ_{SF} = 720 nm). Under these conditions most of the pump energy contribute to form a soliton, which subsequently self-frequency shifts towards the red and approaches the 2ZD point. When sufficient portion of the soliton's spectrum extends across the 2ZD point ($\lambda_{2ZD} = 1560$ nm, which corresponds to SF wavelength of 750 nm) into the normal dispersion region, efficient generation of Cherenkov continuum
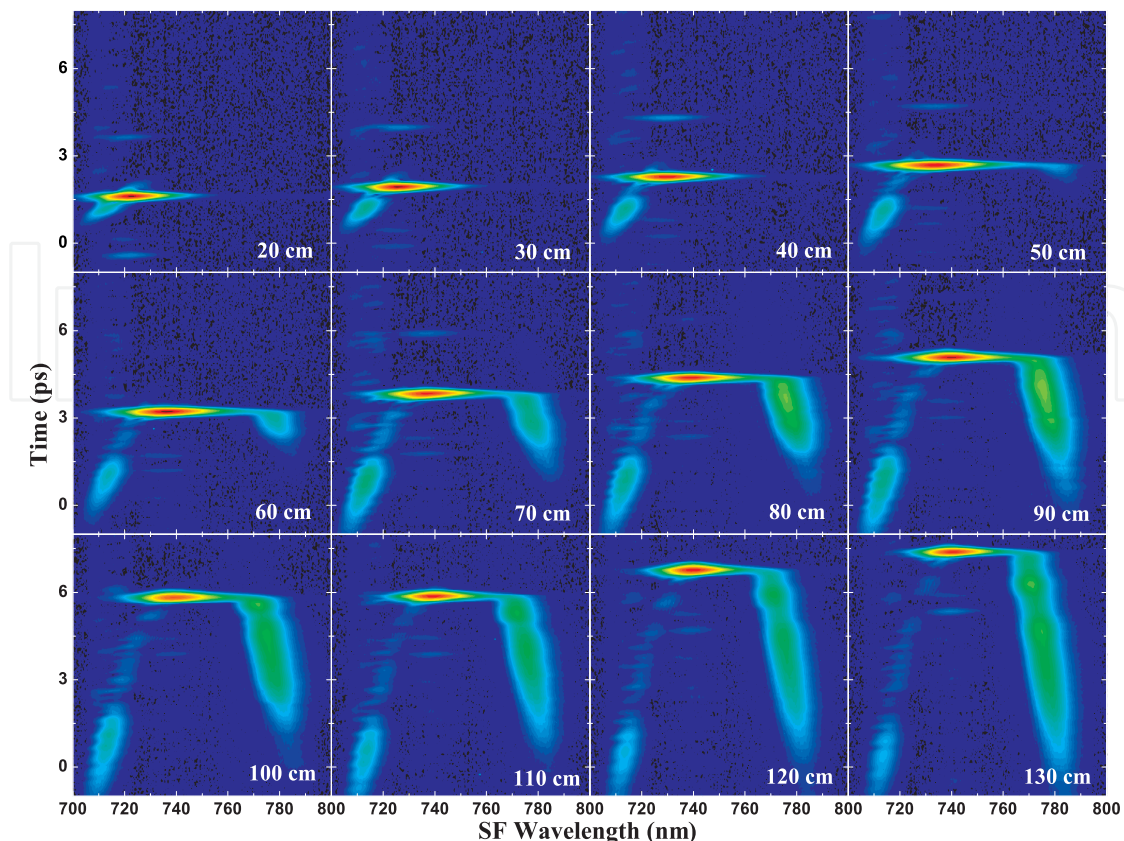
Fig. 7. Experimental X-FROG spectrograms detailing the dynamics of femtosecond soliton propagation in a small-core PCF obtained using a cut-back technique. Input power is held constant corresponding to the fundamental soliton. Raman self-frequency shift seizes as soon as appreciable amount of continuum is generated at about 70 cm. Soliton is slowly loosing energy to the Cherenkov continuum which causes it's spectrum to shrink in width. Color scale is logarithmic.

occurs. In the experimental X-FROG traces of Fig. 7 this continuum manifests itself through a long tail at SF wavelengths longer than 760 nm (1600 nm fundamental) in the normal dispersion region of the fiber. Spectral recoil from the continuum stabilizes the soliton at a wavelength near to the 2ZD point, (after 70 cm of propagation). With further propagation the central wavelength of the soliton remains virtually unchanged due to the appearance of a recoil "force" acting on the soliton's spectrum and balancing the Raman self-frequency shift. Note that there is a continuous energy flow from the soliton to the continuum through uninterrupted spectral overlap (Akhmediev & Karlsson, 1995). Because the soliton is loosing energy to Cherenkov continuum, it's duration must adiabatically increase in order to maintain $N = 1$ soliton number:

$$N^2 \sim \frac{\gamma \cdot E \cdot T_0}{|\beta_2|}, \tag{3}$$

where N is the soliton number, E and T_0 are soliton energy and duration, and β_2 is the dispersion parameter of the fiber. This increase in duration is manifested in spectral width reduction of the soliton in Fig. 7, even though the 100 fs long reference pulse used in these measurements limits the direct temporal resolution of the effect.
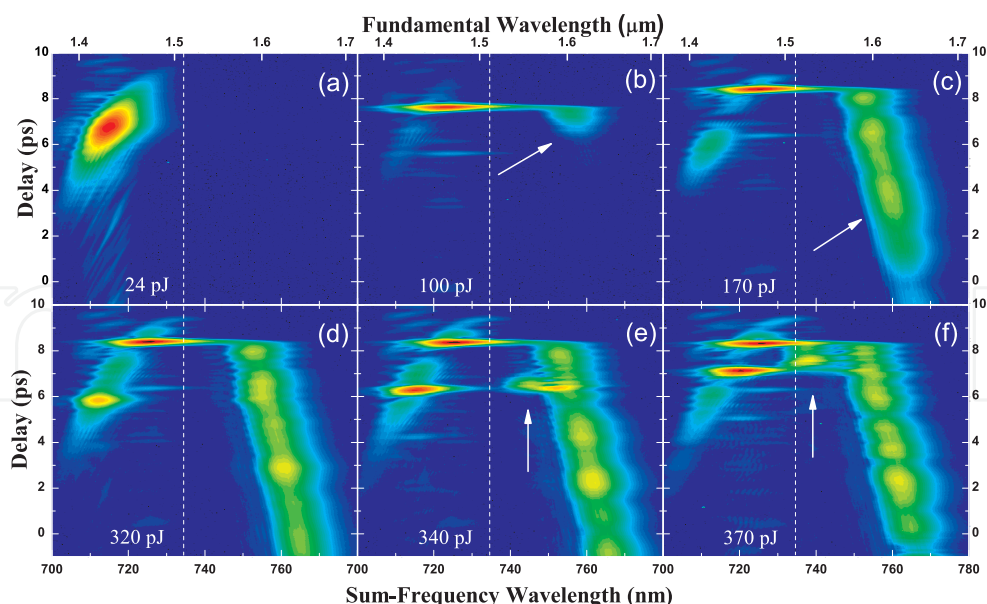
Fig. 8. Power-dependent X-FROG spectrograms measured at the output of a 130 cm-long PCF with $\lambda_{2ZD} = 1510 nm$. The fiber is pumped at 1430 nm, i.e. in the anomalous dispersion region. At lower input powers formation of the primary strong soliton and its Cherenkov radiation are observed, arrows in (b) and (c). Subsequently, a second weaker soliton is formed which interacts with the continuum emitted by the first soliton. The scattering of the Cherenkov radiation by the second soliton leads to energy transfer into a spectral band located between the solitons and the Cherenkov radiation band, arrows in (e) and (f). Vertical dashed line marks 2ZD. Color scale is logarithmic.

More interesting things begin to happen if we increase the input power to the level when two solitons can form from the initial input pulse, Fig. 8. It appears that, contrary to the common belief, the solitons can strongly interact with continuous waves the result of which seems to be the generation of new signals at some non-degenerate frequencies. There is no big surprise here, however, because solitons do not inelastically interact with cw only in integrable systems, described by the standard nonlinear Schrodinger (NLS) equation. Large perturbations either due to dispersion or birefringence change the picture dramatically. As described below, nonintegrability leads to observable and quite spectacular scattering of continuous waves on solitons.

4. Scattering of continuous waves on solitons

Interaction of solitons and continuous waves has been extensively studied in the past. In the framework of standard NLS equation the soliton-cw mixing results in small changes in soliton's position, amplitude and phase. When the cubic dispersion term is included in the propagation equation, the soliton can emit Cherenkov continuum, as described previously. The most recent theoretical analysis (Skryabin & Yulin, 2005), however, predicts the existence of two more phasematched processes in which mixing of a soliton and a cw leads to generation of new spectral components. Physically, the four-wave mixing (FWM) between cws (linear waves) and solitons (nonlinear waves) is different from the textbook case of all-cw FWM (Agrawal, 2001) because the soliton exchanges momentum with other waves as a whole. Therefore, we can no longer associate a particular momentum with a

certain frequency component of the soliton as is possible for a monochromatic cw. From a practical standpoint, the frequency components comprising the soliton's spectrum are dispersionless (see constant group delay within soliton's spectrum in Fig. 3e). Specifically, the wavenumber associated with a certain frequency component of a soliton is a linear function of frequency within the soliton's spectrum $k_{s/\omega}(\omega) = k(\omega_s) + \dfrac{\omega - \omega_s}{v_g(\omega_s)} + \gamma P_s$, where

ω_s is the carrier frequency of the soliton. This same expression enters the phasematching condition for Cherenkov continuum emission, Eq. (2), which in turn is only one of three possible resonances in a more general set of equations for the frequencies of new signal waves generated as a result of soliton-cw interaction:

$$k_{s/sig}(\omega_{sig}) + J\big[\beta_{cw}(\omega_{cw}) - k_{s/cw}(\omega_{cw})\big] = \beta_{sig}(\omega_{sig}) \tag{4}$$

where J can take on three values: 0, -1, and +1. In equation (4), derived using the perturbation theory applied to the generalized NLS equation of propagation, the $J = 0$ case describes the Cherenkov continuum emission and does not include any separate cw pump. The other two nonzero J cases describe the resonances involving a soliton *and* a separate cw pump. Solving these equations yields the frequencies ω_{sig} of newly generated signals. A number of examples were illustrated in the theoretical work (Skryabin & Yulin, 2005) and are not repeated here.

In addition to dispersion, inelastic scattering of a cw on a soliton can be induced by birefringence of the fiber, provided the soliton and the cw pump propagate in orthogonal eigenpolarization states. To account for birefringence, the $J \neq 0$ equations are easily generalized:

$$J = +1: \quad k_{s/sig}^{(x)} - k_{s/cw}^{(x)} = \beta_{sig}^{(y)} - \beta_{cw}^{y} \quad \text{phase-insensitive} \tag{5}$$

$$J = -1: \quad k_{s/sig}^{(x)} + k_{s/cw}^{(x)} = \beta_{sig}^{(y)} + \beta_{cw}^{y} \quad \text{phase-sensitive} \tag{6}$$

where superscripts (x) and (y) denote separate eigenaxes. Physically, the interaction between the orthogonally polarized fields is mitigated by cross-phase modulation terms in the pair of NLS equations written for each eigenpolarization. The phase-matching equations (5) and (6) above are also marked as phase-sensitive and phase-insensitive to highlight the important difference between these two resonances: For the phase-insensitive resonance, both phase and group velocity differences cancel out on the left- and right-hand side of Eq. (5). On the other hand, the phase-sensitive resonance (6) retains the dependence not only on the difference in group velocities, but also the difference in phase velocities between the two eigenaxes of the fiber.

In the experiment of Fig. 8 the signal marked with the arrow in Fig. 8e and f is exactly the result of the resonant interaction of the second soliton with the continuum emitted by the first soliton. Close inspection reveals that the $J = +1$ phase-insensitive resonance is responsible for the emission of the signal at 1.53 μm between the solitons and the Cherenkov tail. The results of numerical modeling for the conditions of the experiment (not shown) were found to match the experimental results nearly perfectly, which further validated the theory of resonant scattering of continuous waves on solitons outlined above.

It is interesting, however, to perform soliton-cw interaction experiments in the most pristine manner, with separate lasers as sources of solitons and continuous waves, thus directly testing the predictions of the theory. To do this, a small-core PCF with 2ZD point at 1510 nm was chosen for its high effective nonlinearity and large dispersion slope to render the system non-integrable due to high-order dispersion. The length of the fiber used was 90 cm. The OPO served as the source of ~100 fs solitons, while the cw field at 1546 nm was generated by a *separate* temperature-controlled laser diode followed by an erbium-doped fiber amplifier. The cw signal is thus located in the normal dispersion region, and the power coupled to the fiber is estimated at ~0.1 W.

The results of this experiment are shown in Fig. 9. The soliton peak power increases from 1.7 to 4.4 to 7 kW for the 1st, 2nd, and 3rd columns respectively. The bottom row in Fig. 9 shows experimental X-FROGs for the case when no cw pump was launched into the fiber. From the top two rows, one can see that as the soliton power increases its interaction with the cw radiation becomes more and more pronounced. There are two reasons for this: The first is that, for this particular phase-insensitive interaction the FWM term responsible for the interaction between the soliton and cw pump is proportional to the modulus squared of the soliton field and only to the first power of the (unconjugated) cw field (Efimov et al., 2005c). Second, and more important, is that, with the increase of the pump power, the soliton
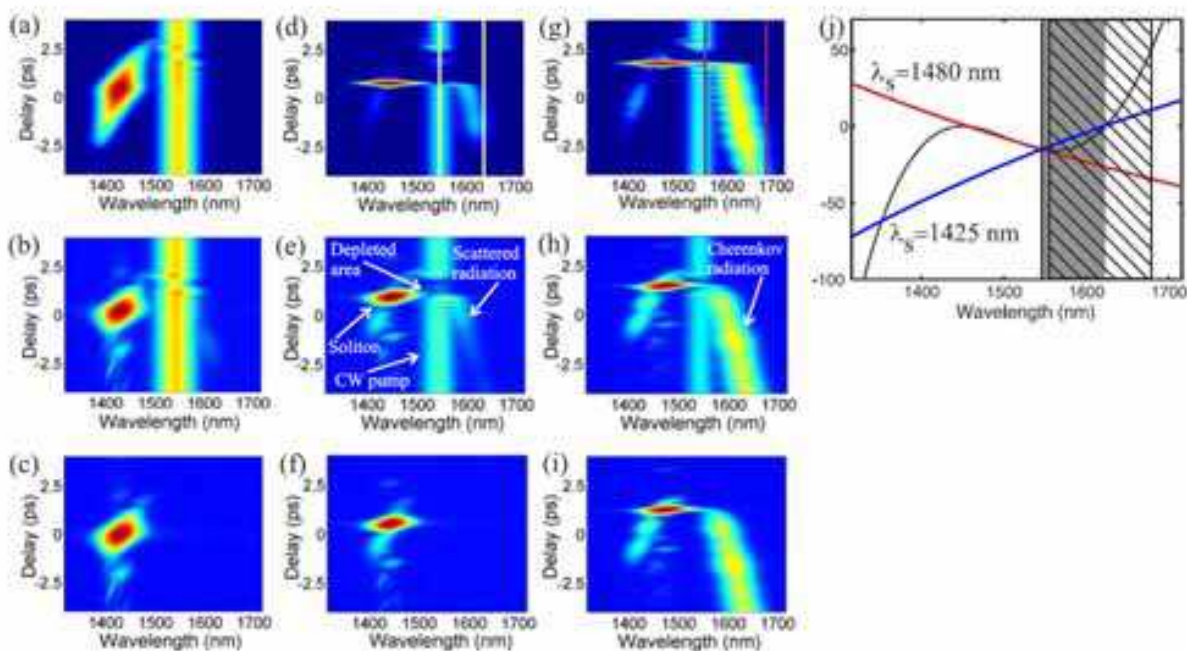

Fig. 9. Interaction between the soliton and cw. First row of spectrograms, (a, d, g)-numerical modeling, second row, (b, e, h)—experimental measurements, and. third row, (c, f, i) shows experimental measurements with the cw pump switched off. 1st, 2nd, and 3rd columns correspond to the soliton peak power 1.7, 4.4, and 7 kW, respectively. Propagation length is 90 cm and cw power is 0.1 W for all the panels. Panel (j) shows the graphical solution to the wave vector matching condition (4) for the two values of the soliton central wavelength. Grey area shows the FWM band, dashed area shows the Cherenkov band. Color scale used in spectrograms is logarithmic.

becomes temporally shorter, and, therefore, the Raman effect brings the soliton closer to the cw frequency, which strongly enhances the efficiency of the FWM process.

Comparison of theoretical and experimental results unambiguously indicates that the frequency component to the longer wavelength side of the cw line in Figs. 9d and e is generated as a result of the $J = +1$ phase-matched FWM between the soliton and the cw pump. When the cw pump is switched off, Fig. 9f, the FWM signal disappears. Another important observation which can be made here is the appearance of the hole in the cw pump; see Figs. 9e and h. This hole is formed because the energy taken from the cw pump is transferred (scattered) by the soliton to the new spectral component.

Conveniently normalized and rescaled geometrical representation of the wave vector matching (4) is shown in Fig. 9j, where the nearly straight lines represent the left-hand side of Eq. (4) for the two different values of the soliton wavelength, and the curved line is the right-hand side of Eq. (4). Since the soliton wavelength is being shifted by the Raman effect, the matching point of the FWM process also shifts with both propagation distance and pump power. The shaded region in Fig. 9j and the white lines in Fig. 9d show the boundaries of the FWM band. The excitation efficiency of the other FWM resonances located to the left of the shaded region is low, and they are not observed in the experiment.

If the input soliton power is made large (third column in Fig. 9) the efficient emission of the Cherenkov continuum by the soliton itself overwhelms the FWM signal, because for this particular PCF the Cherenkov and FWM resonances overlap in large part (see the overlap between the dashed and shaded regions in Fig. 9j). Comparison of Figs. 9g–i clearly shows that this strong radiation is indeed the Cherenkov one, because its emission occurs independently of the cw pump. Thus, in the case when the soliton and cw pump have the same polarizations, observation of the newly generated wave can be achieved only for a relatively small power range of the soliton pump. Other experiments performed using birefringent PCFs help to reveal more details about soliton-cw scattering as well as to observe the other, *phase-sensitive* resonance, described by equation (6).

If the soliton and cw pumps are orthogonally polarized, propagating in a birefringent fiber, then the difference between the phase-sensitive and phase-insensitive scattering should be particularly revealing. This is because the condition of the phase-sensitive resonance depends strongly on the phase velocity difference of the two polarizations, and therefore spectral location of this resonance can be expected to depend strongly on the choice of polarizations for the cw and the soliton pumps. Thus, in what follows we used a commercially available birefringent PCF with a 2.5 μm core. This fiber is anomalously dispersive in the wavelength range of interest around 1.55 μm with third- and higher-order dispersion terms being not important at all. Therefore, the non-integrability of the system, as the key requirement for existence of inelastic soliton-cw scattering, stems here from birefringence, rather than dispersion.

Again, we use separate lasers as sources of solitons and cw. Figure 10 shows the graphical representation of phase-matching conditions (5) and (6) along with experimental and numerical X-FROG spectrograms. Analytical theory predicts in Fig. 10a that the locations of phase-sensitive and phase-insensitive resonances differ significantly depending on whether cw propagates in the fast fiber axis and the soliton—in the slow axis, or vice versa. In the experiment the cw and femtosecond beams were orthogonally polarized and launched into a 24 cm long piece of PCF by use of a polarizing cube. At the output of the PCF the cw eigenaxis is selected with another polarizer, thus strongly, but not completely damping the cross-correlation signal from the soliton. Figure 10b shows the X-FROG trace for the case

when the soliton central wavelength is 1430 nm and the input power is adjusted such that the stimulated Raman scattering shifts the soliton spectrum by no more than 10 nm.

Let us assume that the soliton is x-polarized and the cw is y-polarized. The theory predicts that the waves generated as a result of the FWM interaction between the orthogonally polarized soliton and the cw retain the cw polarization. The source of the FWM signal for the phase-insensitive resonance (5) is the $\left|A_x^2\right|A_y$ term, whereas the phase-sensitive resonance (6) is due to the $A_x^2 A_y^*$ term in the generalized NLS equation:

$$
\begin{aligned}
\left[i\partial_z + D_{x,y}\left(i\partial_t\right)\right]A_{x,y} &+ \gamma\left[\left|A_{x,y}\right|^2 + \frac{2}{3}\left|A_{y,x}\right|^2\right]A_{x,y} + \\
&+ \frac{\gamma}{3}A_{y,x}^2 A_{x,y}^* + \gamma A_{x,y}\int dt' R(t') I(t-t',z) = 0,
\end{aligned}
\tag{7}
$$

where $A_{x,y}$ are the field amplitudes in orthogonal polarizations, $I = \left|A_x\right|^2 + \left|A_y\right|^2$ is the intensity, γ is the nonlinear coefficient, $R(t)$ is the standard Raman response (Agrawal, 2001), and $D_{x,y}(i\partial_t)$ are the dispersion operators, specific for each eigenaxis where constant (phase velocity) and linear (group velocity) Taylor expansion terms are appropriately included.

The graphical solutions, Fig. 10a, to the wave-vector matching equations (5) and (6) indicate that for a soliton at 1430 nm central wavelength, both resonances are located near 1350 nm for one set of launching conditions. If, however, the eigenaxes are swapped, the phase-sensitive resonance disappears, while phase-insensitive resonance remains in the vicinity of the soliton. Experiments indeed reveal the presence of the signal at 1350 nm for one set of input launching conditions. If the eigenaxes are swapped, then the signal disappears from the picture, Fig. 10d. The numerically computed X-FROG trace showing the FWM signal, Fig. 10c matches nearly perfectly the experimental one, Fig 10b. These and other evidence (Efimov et al., 2006) verify the observation of phase-sensitive resonance in scattering of a continuous wave on a soliton in a typical birefringent PCF.

It is important to note that the observation of a subpicosecond structure in a truly cw wave, as the result of resonant interaction with a soliton, or otherwise, is highly nontrivial from the experimental standpoint and has not been demonstrated before. X-FROG appears to be a very potent technique for a wide spectrum of time-frequency-resolved measurements, including measuring the temporal structure of separate continuous wave beams. As described below, careful broadband X-FROG measurements can resolve previously obscure features in supercontinua, generated in PCFs. There, we will see the effects of inelastic soliton-cw interaction as an important element of supercontinuum dynamics during its formation and propagation in the fiber.

5. Supercontinuum generation in a highly nonlinear soft glass PCF

The success of silica photonics crystal fibers, which offered new degrees of freedom to manipulate dispersion and nonlinear properties, inspired the exploration of other glass materials as the host for these structures. Currently, such materials as polymers (van Eijkelenborg et al., 2001), highly-nonlinear glasses (Ravi Kanth Kumar et al., 2002) and even quantum dot-doped matrices (Yu et al., 2007) are being used to manufacture PCFs. The
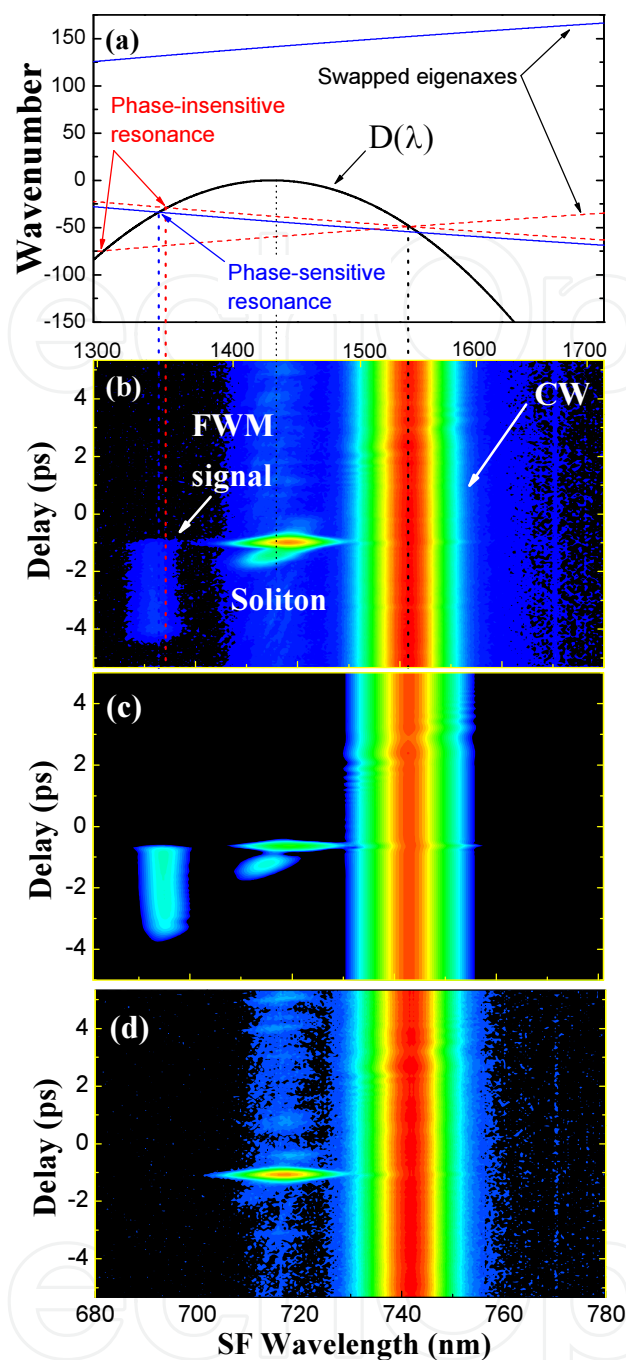
Fig. 10. (a) Graphical solutions to the wave-vector matching equations (5) and (6). Wavelengths of the expected FWM signals are given by the intersections of the quasi-parabolic function, describing the dispersion of linear waves, with the straight lines. The solid (dashed) curves correspond to the phase-sensitive (phase-insensitive) resonance; see the text for details. (b) Experimental X-FROG spectrogram showing generation of the new spectral component near 1350 nm. (c) Numerically generated X-FROG diagram corresponding to the experimental conditions of (b). (d) Experimental X-FROG diagram showing no new spectral components when polarizations of the soliton and cw are swapped. The blob between the signal and the cw in (b)–(d) is a small part of the soliton power coupled to the orthogonal polarization.

diversity of the modern PCF family is truly spectacular. The urgent need to study the dynamics of optical signals in these structures in time-frequency can be addressed with X-FROG.

Recently developed extrusion-based PCFs made from soft glasses, such as Schott SF6, can be about an order of magnitude more nonlinear as compared to their silica counterparts. Indeed, recent supercontinuum generation experiments in these SF6 PCFs indicate that a multioctave continuum can be generated efficiently in only millimeters of fiber using 100 fs pulses at telecom wavelengths and nanojoule energies (Omenetto et al., 2006). Previous measurements of supercontinua in time-frequency suffered from low signal-to-noise ratio and thus could not be directly compared to numerical results (Dudley et al., 2002). Nevertheless, low-noise broadband measurements with X-FROG are possible and may look almost indistinguishable from the numerically generated spectrograms.

Figure 11 shows theoretically and experimentally produced spectrograms of a supercontinuum pulse generated in a 11 cm long sample of extruded SF6 PCF using the X-FROG system described in Section 2. Input pump pulse is of typical 100 fs duration centered at 1550 nm. The fact that the broadband radiation in general lies on the parabola, which corresponds to the group delay as a function of wavelength, immediately tells us that all of the supercontinuum spectrum is generated at the very beginning of the fiber, supporting the previous findings (Omenetto et al., 2006). Subsequent propagation is, in fact, nearly purely dispersive. If the normal dispersion side of the experimental spectrogram (shorter wavelengths) matches the numerical one nearly perfectly, we see a clear discrepancy on the anomalous side of the picture, where solitons are formed. It appears that the experimental solitons are elongated in time. Notwithstanding the fact that the red-most numerical soliton is also stretched (due to steep confinement loss beyond 1700 nm), the explanation is, in fact, the temporal jitter associated with the presence of slight envelope modulations on the pump pulse (Efimov & Taylor, 2008).
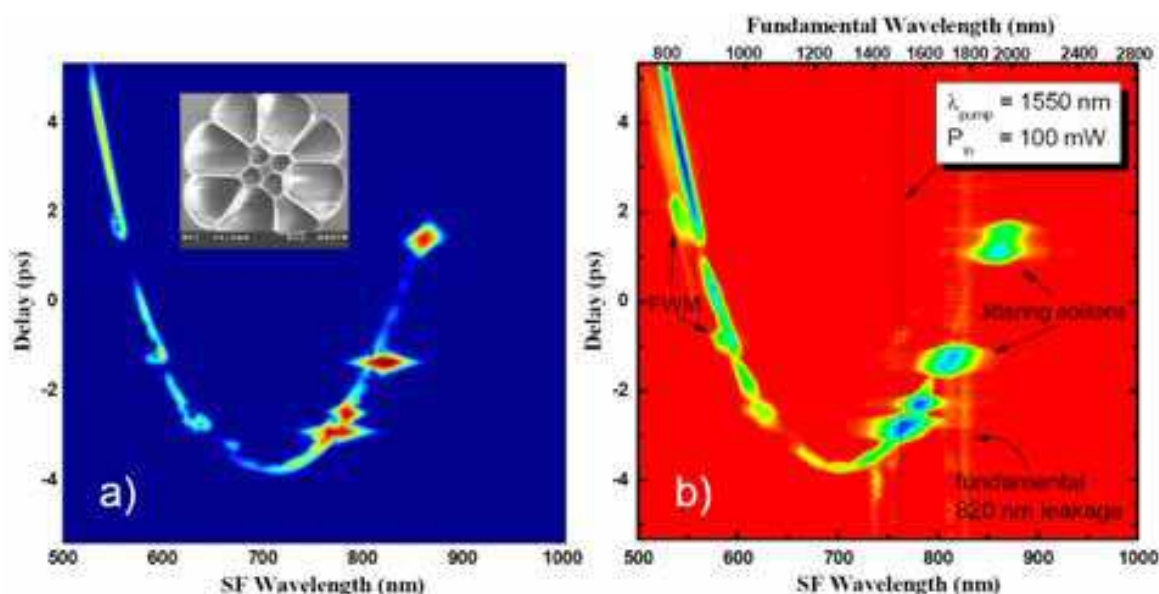

Fig. 11. Numerical (a) and experimental (b) X-FROG spectrograms of a supercontinuum pulse at the output of 11 cm long piece of SF6 PCF. Lower axis is sum-frequency and upper axis in (b) – fundamental wavelength of the signal. Color scale is logarithmic covering 30 dB of signal intensity. Inset shows the SEM image of the fiber tip
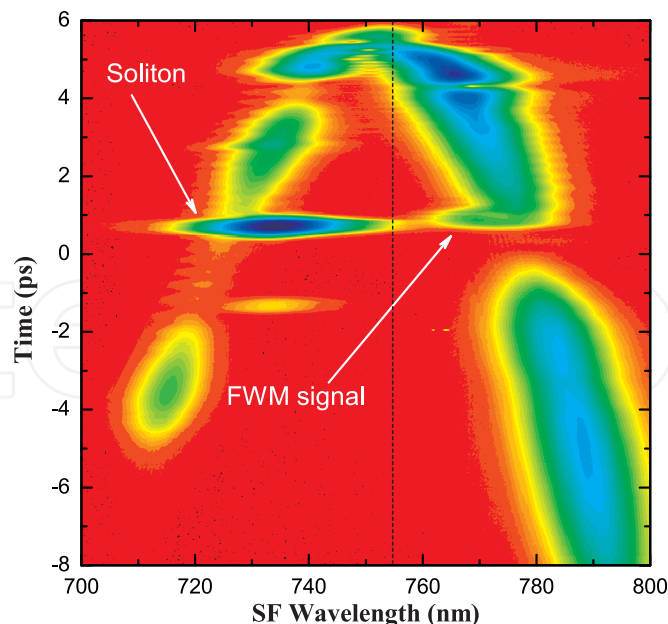
Fig. 12. Experimental X-FROG spectrogram showing the dynamics of the continuum in the vicinity of the 2ZD point of a small-core *silica* PCF from Fig. 6. The PCF is pumped exactly at 2ZD point (vertical dashed line). Dispersion is anomalous at shorter wavelengths and normal at longer wavelengths. A soliton forms on the anomalous side and interacts with the quasi-cw continuum on the normal dispersion side, which rresults in FWM signal generation (arrow). Color scale is logarithmic.

Nevertheless, the agreement between the theory and experiment is remarkable. On the normal dispersion side (shorter wavelengths) the quasi-continuum is pierced with holes directly opposite to solitons. The missing radiation is scattered in the FWM signals as the result of soliton-cw interaction, described in the previous section. As is mentioned in (Skryabin & Yulin, 2005) the group velocity-matched propagation of a soliton and a cw, located on both sides of ZD point, leads to the formation of a temporal hole in the cw, directly opposite to soliton. In the current experiment, however, the soliton undergoes slow Raman self-frequency shift during propagation so that it's carrier wavelength becomes progressively longer and thus group velocity—slower. Careful consideration of the phase-matching condition (4) shows that the FWM signal will appear at wavelengths shorter than cw, as is observed in both experimental and numerical spectrograms in Fig. 11.

Interestingly, if we were to study the continuum formation in the vicinity of the second dispersion zero (of a different PCF), a similar effect is observed, Fig. 12, except that in this case the soliton shifts towards inside the "parabola" and the FWM signal also appears inside, in total agreement with the analytical theory and numerical computations.

6. Solitons and continuum generation in all-glass bandgap PCF

Continuing technical advancement in the area of complex fiber design recently resulted in the development of a new class of all-glass PCFs (Feng et al., 2003; Luan et al., 2004). These fibers consist of an arrangement of glass rods embedded in a background matrix of a different glass and no air channels. Depending on the index difference between the rods and the background these fibers will display either index guiding or resonant bandgap guiding

characteristics (Litchinitser et al., 2002). For the latter case the rods would have higher index (e.g. Ge-doped silica) than the background (e.g. pure silica). Such a design offers an alternative to liquid-filled PCFs (Larsen et al., 2003). The transmission spectra of these resonant-guiding PBFs consist of multiple low-loss bandgaps separated by high-attenuation regions. Importantly, in each bandgap the dispersion varies from normal to anomalous with increasing wavelength. Thus, each bandgap can support both solitons and dispersive waves (Fuerbach et al., 2005).

Moreover, intricate cross-bandgap phase-matching conditions can be realized, e.g. for the process of Four-Wave Mixing (FWM) as was recently predicted (Rasmussen et al., 2008). These intricate interactions can be revealed using time-spectral visualisation techniques as described previously. One complication arises, however: Typically, all-solid PBF designs are not well-suited for studies of nonlinear-optical interactions because of relatively large core sizes with effective mode areas on the order of tens of square micrometers. Thus, at best a single soliton formation can be observed with just oscillator pumping (Fuerbach et al., 2005). The observation of nonlinear cross-bandgap processes will thus require amplified pulses.

The fiber used in our experiments is similar to the one described in (Wang et al., 2006) and consists of a triangular array of Ge-doped glass rods embedded in a pure silica background (index difference $\Delta n = 0.033$). The cladding pitch and rod diameter are $\Lambda = 6.5\ \mu m$ and $d = 3.0\ \mu m$ respectively. The guiding region is defined by six rods surrounding a pure silica central region. The fiber structure in the vicinity of the core and its spectral transmission are shown in Fig. 13.
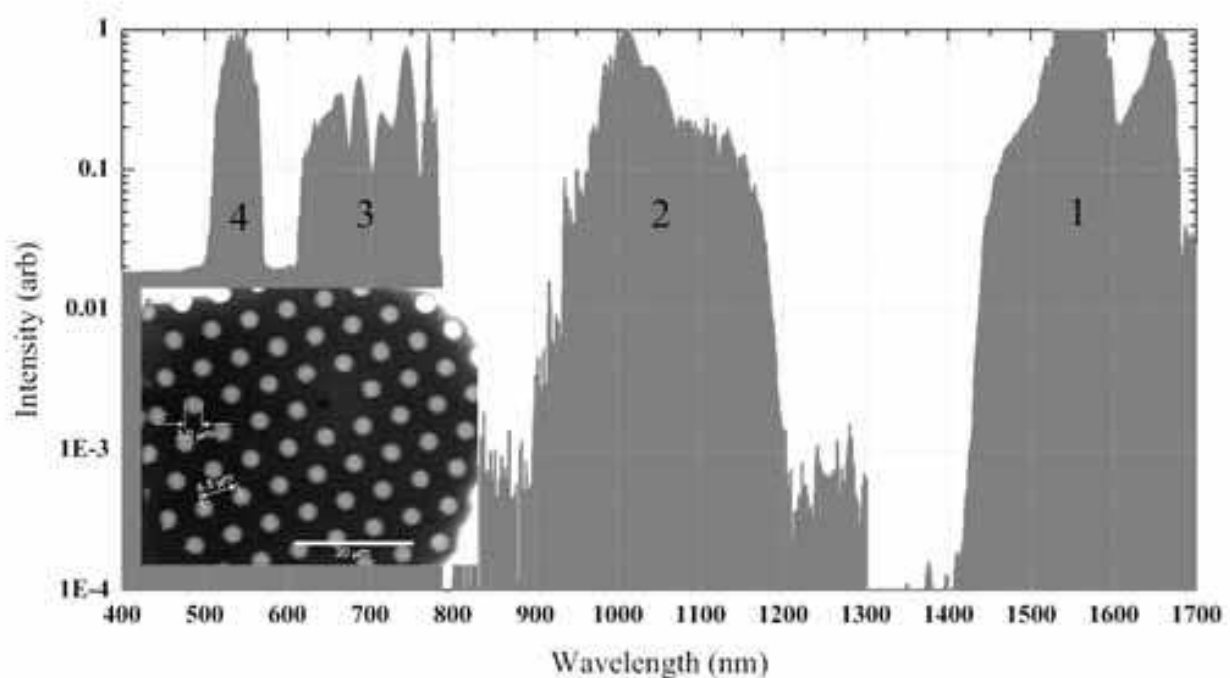

Fig. 13. Spectral transmission of the all-glass PBF. The structure of the transmission bands reflects the non-uniform spectral shape of the continuum used for their measurement. Bandgaps marked 1, 2, 3, and 4, and their edges can be clearly identified. Inset shows the SEM image of the central region fiber cross-section with rod diameter d and pitch Λ identified
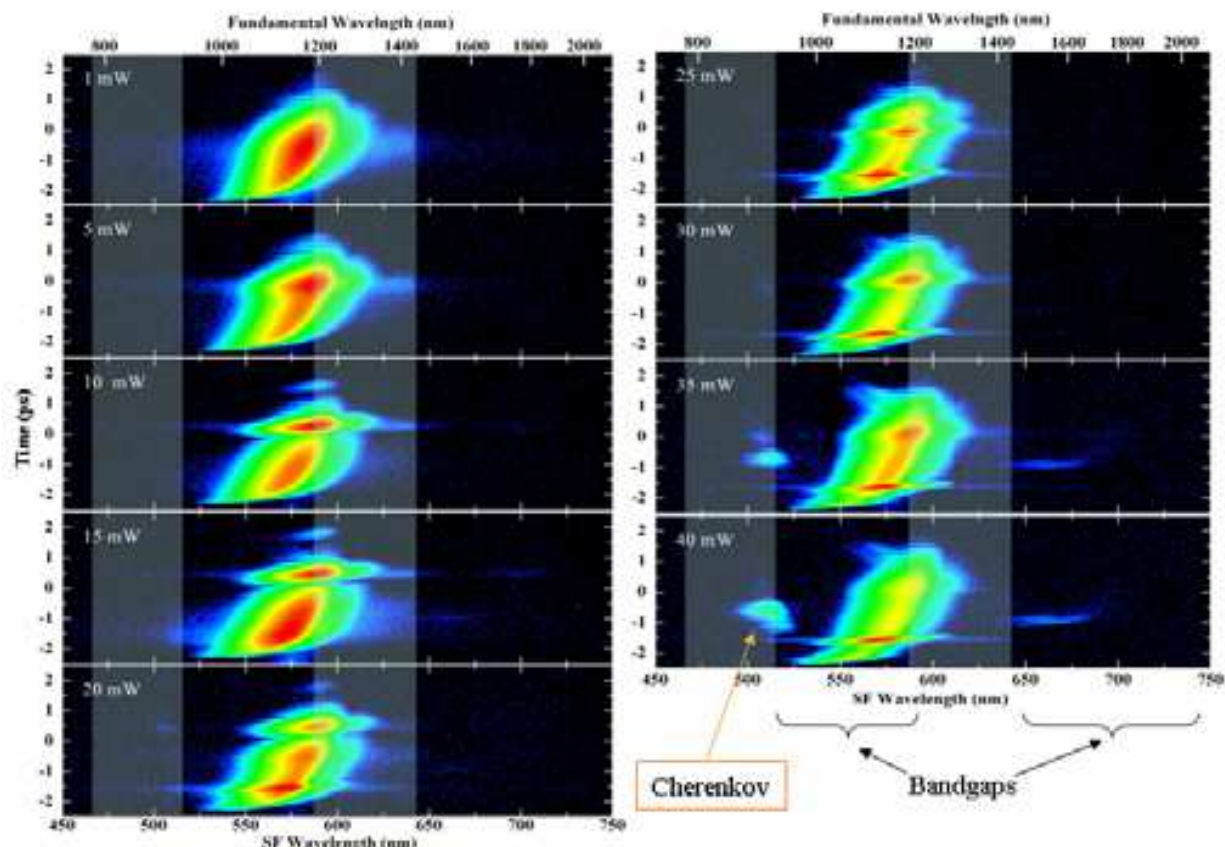
Fig. 14. Sequence of experimental X-FROG traces for varying input pump powers ranging from 4 nJ(1 mW input average power) to 160 nJ (40 mW) as indicated. Semi-transparent regions mark the high-loss interbandgap space. Color scale is logarithmic spanning 40 dB of sum-frequency signal.

To be able to access higher pump pulse intensities the fiber was pumped with 50 fs pulses at 1150 nm central wavelength from a laser, regenerative amplifier and optical parametric amplifier system (250 kHz Coherent Mira-RegA-OPA). At the output of 21 cm long fiber sample the optical pulses are analyzed with a SFG X-FROG system similar to the one described in Section 2, except that a KDP crystal was used instead of BBO in order to increase even further the phase-matching bandwidth to cover 500 to 2000 nm wavelength span.

Previous FROG measurements in a liquid-filled PCF revealed the formation of a soliton and generation of a phase-matched Cherenkov wave in the same bandgap (Fuerbach et al., 2005). Fig. 14 shows a sequence of X-FROG traces measured at the output of our all-glass PBF for different input pulse energies. Because the dispersion varies substantially over the bandwidth of the input pulse, only a fraction of the input spectrum on the red side contributes to the first soliton. This soliton forms very close to the edge of the bandgap and being pushed to longer wavelength by the stimulated Raman scattering, responsible for the soliton self-frequency shift, efficiently looses energy and disappears. The behavior of the second soliton is very similar: it forms at 25 mW input power, then elongates at 35 mW and finally disappears at 40 mW. The fact that these solitons do not extend their spectrum over to the normal dispersion region at wavelengths shorter than 1000 nm explains why the Cherenkov continuum appears only when the third soliton forms. This soliton propagates

with its spectrum situated further away from the bandgap edge so that it is not affected by the loss as much. As a result, its duration is much shorter than that of the first two solitons and the blue edge of its spectrum extends over to the normal dispersion side making it possible to emit the Cherenkov continuum.

The result of this analysis shows that the presence of a substantial loss on one side of the soliton's spectrum, e.g. due to the bandgap edge, limits the extent of not only the affected side, but also the opposite side of the spectrum. This is expected because within a soliton, being a nonlinear wave, the spectral components are not independent, as is the case for a dispersive wave. The immediate consequence of this result is that the Cherenkov emission in a bandgap fiber is less efficient than that in more traditional waveguides. Only when pumped very close to the dispersion zero the radiation of the Cherenkov wave can be effective.

At higher pump powers one can also observe generation of visible radiation around 650 and 550 nm, which reside within the next two higher-order bandgaps. Fig. 15 presents the X-FROG spectrogram under these conditions. Here the pump wavelength is set to 1125 nm, i.e. closer to ZDW so the Cherenkov continuum is more prominent. More importantly, however, the time-spectral structure of the visible components in the two higher-order bandgaps is uncovered. The shape of the trace in the 550 nm bandgap, as well as the nearly-uniform illumination of the fiber suggests that the emission occurred at the very beginning of the fiber. Group delay differences between different bandgaps can be directly determined from the trace of Fig. 3 and show expected dependence on the bandgap number: Shorter
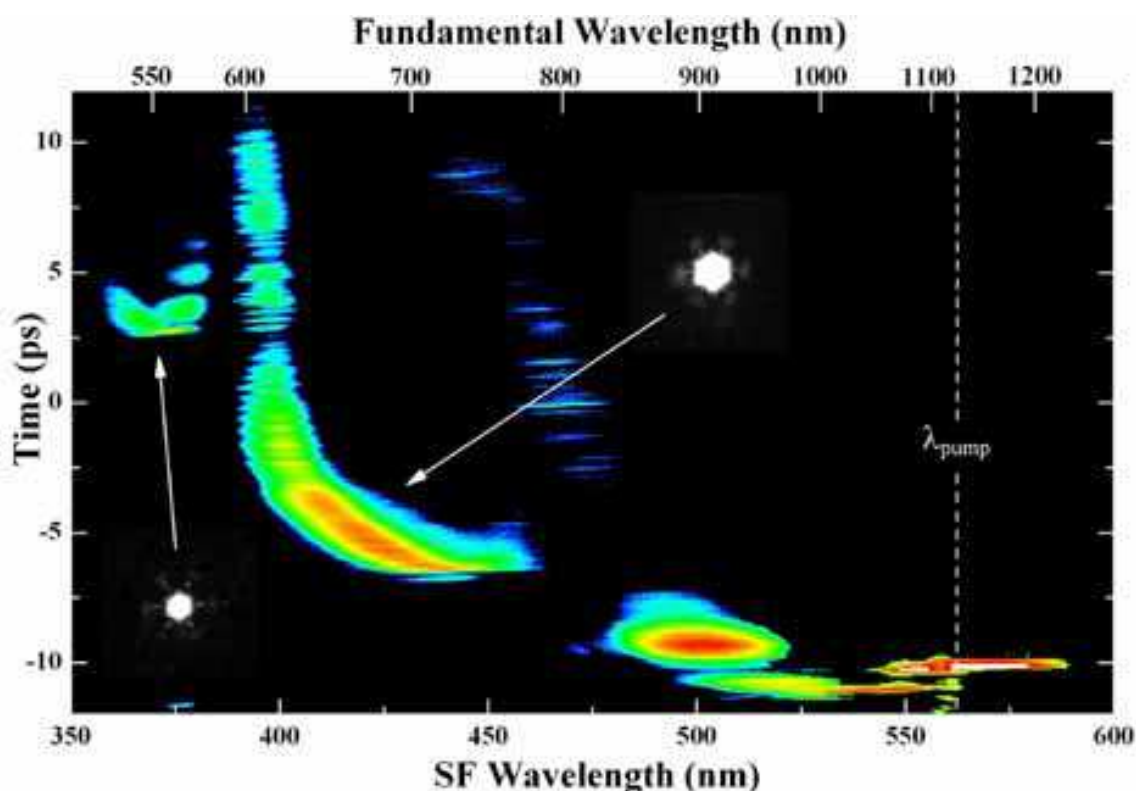

Fig. 15. Experimental X-FROG trace showing time-spectral properties of the signals in three bandgaps (number 2, 3, and 4 in Fig. 13) simultaneously. Insets show the near-field intensity distribution of the modes nonlinearly generated in bandgaps 3 and 4, as marked by arrows. Gray/color scale is logarithmic spanning 35 dB of sum-frequency signal.

wavelength bandgaps are delayed with respect to the longer ones (Rasmussen et al., 2008). Insets show the optical near-field images of the generated visible modes and indicate fundamental mode profiles at both wavelengths.

The observed interbandgap generation may involve two mechanisms, working separately or simultaneously. First, the input pulse may generate a broadband continuum due to the usual mechanisms (self-phase modulation, soliton compression and fission, dispersive wave generation) at the very beginning of the fiber and the resulting spectral components fill in the bandgaps, where they propagate dispersively with minimal loss. In addition, phase-matched inter-bandgap FWM generation may play a role in the observed behavior (Rasmussen et al., 2008). Previously, intermodally phase-matched FWM (Stolen & Leibolt, 1976; Akimov et al., 2003) as well as third harmonic generation (Efimov & Taylor., 2005b) were observed in both regular fibers and PCFs. Inter-bandgap phase-matched FWM is a very similar process and thus appears likely to contribute to the generation mechanism. Complete modeling of the PBF fiber structure as well as further experiments are needed to fully understand the observed phenomena.

7. Conclusion

Thorough understanding of fundamental nonlinear processes occurring as optical signals propagate along a waveguide require obtaining as much experimental information as possible. It was recognized a long time ago (Treacy, 1971) that spectrogram representation of optical pulses, that is 2D plots of signal amplitude in time and frequency showing relative temporal positions of different frequency components comprising the pulse, is, in fact, the most intuitive and rich way to describe the pulse. Simultaneous temporal and spectral resolution, limited only by the fundamental Fourier relation, gives unprecedented clarity of images, substantially simplifying the interpretation of the data and allowing visual comparison with theory and numerical modeling. An experimental tool such as X-FROG being slightly more involved in implementation than spectral or autocorrelation-type systems will reward one with the most dramatic images of nonlinear evolution of ultrashort pulses in optical fibers and waveguides. As often happens, however, when new advances in experimental techniques mature, they bring to light not only answers to long-standing questions, but create new puzzles to challenge both theorists and experimentalists alike.

In this work the emphasis was placed on visualizing and studying various aspects of soliton dynamics in regular and photonic crystal fibers and their interaction with dispersive waves. Recent analytical theory explains well all the resonant soliton-cw scattering processes observed in the experiments described in sections 3 and 4. This scattering of cw on solitons in non-integrable systems, either due to high-order dispersion or birefringence, leads to generation of new non-degenerate signals, which were observed and confirmed numerically. These processes are important, for example, in supercontinuum generation, where quasi-cw radiation propagating in the normal dispersion region interacts with Raman-shifting solitons formed on the anomalous side (section 5). Broadband and high dynamic range X-FROG measurements of supercontinua show excellent agreement with numerics, as well as directly show experimental artifacts, such as timing jitter of solitons.

We also obtained most clear images of well-known nonlinear processes such as soliton formation in long lengths of regular fiber and Raman solitons in silica cobweb photonic crystal fibers (section 2). Among other things, this brings about the educational value of X-FROG measurements and presentation of numerical results.

Finally, X-FROG measurements of multiple soliton formation and nonlinear cross-bandgap generation in all-glass PBFs challenge the current state of affairs in our understanding of very complex nonlinear-optical interactions occurring in waveguiding structures. Further discoveries can be expected by applying the X-FROG technique to the investigation of ultrafast nonlinear optical processes in other types of photonic crystal structures, complex waveguides and other nonlinear systems.

8. References

Agrawal, G. P. (2001). Nonlinear Fiber Optics. Academic Press, San Diego.

Akhmediev, N. & Karlsson, M. (1995). Cherenkov radiation emitted by solitons in optical fibers. *Physical Review A* Vol. 51, No. 3, pp. 2602-2607.

Akimov, D. A.; Serebryannikov, E. E.; Zheltikov, A. M.; Schmitt, M.; Maksimenka, R.; Kiefer, W.; Dukel'skii, K. V.; Shevandin, V. S. & Kondrat'ev, Yu. N. (2003). Efficient anti-Stokes generation through phase-matched four-wave mixing in higher-order modes of a microstructure fiber. *Optics Letters* Vol. 28, No. 20, pp. 1948-1950.

Biancalana, F.; Skryabin, D. V. & Yulin, A. V. (2004). Theory of the soliton self-frequency shift compensation by the resonant radiationin photonic crystal fibers. *Physical Review E* Vol. 70, No. 1 016615-1:9.

Birks, T. A.; Wadsworth, W. J. & Russell, P. St. J. (2000). Supercontinuum generation in tapered fibers. *Optics Letters* Vol. 25, No. 19, pp. 1415-1417.

Chen, Z.; Taylor, A. J. & Efimov, A. (2009). Coherent mid-infrared broadband continuum generation in non-uniform ZBLAN fiber taper. *Optics Express* Vol. 17, No. 7, pp. 5852-5860.

Dudley, J. M.; Gu, X.; Xu, L.; Kimmel, M.; Zeek, E.; O'Shea, P.; Trebino, R. Coen, S. & Windeler, R. S. (2002). Cross-correlation frequency resolved optical gating analysis of broadband continuum generation in photonic crystal fiber: simulations and experiments. *Optics Express* Vol. 10, No. 21, pp. 1215-1221.

Dudley, J. M.; Genty, G. & Coen, S. (2006). Supercontinuum generation in photonic crystal fiber. *Reviews of Modern Physics* Vol. 78, No. 4, pp. 1135-1185.

Efimov, A.; Taylor, A. J.; Omenetto, F. G.; Yulin, A. V.; Joly, N.; Biancalana, F.; Skryabin, D. V.; Knight, J. C. & Russell, P. St. J. (2004). Time-spectrally-resolved ultrafast nonlinear dynamics in small-core photonic crystal fibers: Experiment and modelling. *Optics Express* Vol. 12, No. 26, pp. 6498-6507.

Efimov, A. & Taylor, A. J. (2005a). Cross-correlation frequency-resolved optical gating for studying ultrashort-pulse nonlinear dynamics in arbitrary fibers. *Applied Optics* Vol. 44, No. 20, pp. 4408-4411.

Efimov, A. & Taylor, A. J. (2005b). Spectral-temporal dynamics of ultrashort Raman solitons and their role in third-harmonic generation in photonic crystal fibers. *Applied Physics B* Vol. 80, No. 6, pp. 721-725.

Efimov, A.; Yulin, A. V.; Skryabin, D. V.; Knight, J. C.; Joly, N.; Omenetto, F. G.; Taylor, A. J. & Russell, P. St. J. (2005c). Interaction of an Optical Soliton with a Dispersive Wave *Physical Review Letters* Vol. 95, No. 21, pp. 213902-1:4.

Efimov, A.; Taylor, A. J.; Yulin, A. V.; Skryabin, D. V. & Knight, J. C. (2006). Phase-sensitive scattering of a continuous wave on a soliton. *Optics Letters* Vol. 31, No. 11 1624-1626.

Efimov, A. & Taylor, A. J. (2008) Supercontinuum generation and soliton timing jitter in SF6 soft glass photonic crystal fibers. *Optics Express* Vol. 16, No. 8, pp. 5942-5953.

van Eijkelenborg, M. A.; Large, M. C. J.; Argyros, A.; Zagari, J.; Manos, S.; Issa, N. A.; Bassett, I.; Fleming, S.; McPhedran, R. C.; de Sterke, C. M. & Nicorovici1, N. A. P. (2001). Microstructured polymer optical fibre. *Optics Express* Vol. 9, No. 7, pp. 319-327.

Feng, X.; Monro, T. M.; Petropoulos, P.; Finazzi, V. & Hewak, D. (2003). Solid microstructured optical fiber. Optics Express Vol. 11, No. 18, pp. 2225-2230.

Fuerbach, A.; Steinvurzel, P.; Bolger, J. A. & Eggleton, B. J. (2005). Nonlinear pulse propagation at zero dispersion wavelength in anti-resonant photonic crystal fibers *Optics Express* Vol. 13, No. 8, pp. 2977-2987.

Genty, G.; Lehtonen, M.; Ludvigsen, H. & Kaivola, M. (2004). Enhanced bandwidth of supercontinuum generated in microstructured fibers. *Optics Express* Vol. 12, No. 15, pp. 3471-3480.

Harbold, J. M.; Ilday, F. O.; Wise, F.; Birks, T. A.; Wadsworth, W. J. & Chen, Z. (2002). Long-wavelength continuum generation about the second dispersion zero of a tapered fiber. *Optics Letters* Vol. 27, No. 17, pp. 1558-1560.

Hilligsøe, K. M.; Andersen, T. V.; Paulsen, H. N.; Nielsen, C. K.; Mølmer, K.; Keiding, S. R.; Kristiansen, R.; Hansen, K. P. & Larsen, J. J. (2004). Supercontinuum generation in a photonic crystal fiber with two zero dispersion wavelengths. *Optics Express* Vol. 12, No. 6, pp. 1045-1054.

Hori, T.; Nishizawa, N.; Goto, T.; & Yoshida, M. J. (2003). Wideband and nonmechanical sonogram measurement by use of an electronically controlled, wavelength-tunable, femtosecond soliton pulse. *Journal of the Optical Society of America B* Vol. 20, No. 11, pp. 2410-2417.

Hori, T.; Nishizawa, N. & Goto, T. (2004). Experimental and numerical analysis of widely broadened supercontinuum generation in highly nonlinear dispersion-shifted fiber with a femtosecond pulse. *Journal of the Optical Society of America B* Vol. 21, No. 11, pp. 1969-1980.

Jones, D. J.; Diddams, S. A.; Ranka, J. K.; Stentz, A.; Windeler, R. S.; Hall, J. L. & Cundiff, S. T. (2000). Carrier-Envelope Phase Control of Femtosecond Mode-Locked Lasers and Direct Optical Frequency Synthesis. *Science* Vol. 288, No. 5466, pp. 635-639.

Karpman, V. I. (1993). Radiation by solitons due to higher-order dispersion. *Physical Review E* Vol. 47, No. 3, pp. 2073-2082.

Knight, J. C.; Birks, T. A.; Russell, P. St. J. & Atkin, D. M. (1996). All-silica single-mode optical fiber with photonic crystal cladding. *Optics Letters* Vol. 21, No. 19, pp. 1547-1549.

Knight, J. C. (2003). Photonic crystal fibers. *Nature* Vol. 424, No. 6950, pp. 847-851.

Larsen, T. T.; Bjarklev, A.; Hermann, D. S. & Broeng, J. (2003) Optical devices based on liquid crystal photonic bandgap fibres. *Optics Express* Vol. 11, No. 20, pp. 2589-2596.

Lin, C.; Nguyen, V. T. & French, W. G. (1978). Wideband near-IR continuum (0.7-2.1 μm) generated in low-loss optical fibres. *Electronics Letters* Vol. 14, No. 25, pp. 822-823.

Linden, S.; Giessen, H. & Kuhl, J. (1998). XFROG - A New Method for Amplitude and Phase Characterization of Weak Ultrashort Pulses. *Physica Status Solidi (b)*, Vol. 206, No. 1, pp. 119-124.

Litchinitser, N. M.; Abeeluck, A. K.; Headley, C. & Eggleton, B. J. (2002) Antiresonant reflecting photonic crystal optical waveguides. *Optics Letters* Vol. 27, No. 18, pp. 1592-1594.

Lu, F.; Deng, Y. & Knox, W. H. (2005). Generation of broadband femtosecond visible pulses in dispersion-micromanaged holey fibers. *Optics Letters* Vol. 30, No. 12, pp. 1566-1568.

Luan, F. George, A. K.; Hedley, T. D.; Pearce, G. J.; Bird, D. M. Knight, J. C. & Russell, P. St. J. (2004). All-solid photonic bandgap fiber. *Optics Letters* Vol. 29, No. 20, pp. 2369-2371.

Morioka, K.; Mori, K.; Kawanishi, S. & Saruwatari, M. (1994). Pulse-width tunable, self-frequency conversion of short optical pulses over 200 nm based on supercontinuum generation. *Electronics Letters* Vol. 30, No. 23, pp. 1960-1962.

Nishizawa, N. & Goto, T. (2001). Experimental analysis of ultrashort pulse propagation in optical fibers around zero-dispersion region using cross-correlation frequency resolved optical gating. *Optics Express* Vol. 8, No. 6, pp. 328-334.

Omenetto, F. G.; Wolchover, N. A.; Wehner, M. R.; Ross, M.; Efimov, A.; Taylor, A. J.; Ravi Kanth Kumar, V. V.; George, A. K.; Knight, J. C.; Joly, N. Y. & Russell, P. St. J. (2006). Supercontinuum Generation in Sub-Centimeter Lengths of High-Nonlinearity Photonic Crystal Fibers. *Optics & Photonics News* Vol. 17, December 2006, p. 35.

Ranka, J. K.; Windeler, R. S. & Stentz, A. J. (2000). Visible continuum generation in air-silica microstructure optical fibers with anomalous dispersion at 800 nm. *Optics Letters* Vol. 25, No. 1, pp. 25-27.

Rasmussen, P. D.; Laegsgaard, J. & Bang, O. (2008). Degenerate four wave mixing in solid core photonic bandgap fibers. *Optics Express*, Vol. 16, No. 6, pp. 4059-4068.

Ravi Kanth Kumar, V. V.; George, A. K.; Reeves, W. H.; Knight, J. C.; Russell, P. St. J.; Omenetto, F. G. & Taylor, A. J. (2002). Extruded soft glass photonic crystal fiber for ultrabroad supercontinuum generation. *Optics Express* Vol. 10, No. 25, pp. 1520-1525.

Skryabin, D. V.; Luan, F.; Knight, J. C. & Russell, P. St. J. (2003). Soliton Self-Frequency Shift Cancellation in Photonic Crystal Fibers. *Science* Vol. 301, No. 5640, pp. 1705-1798.

Skryabin, D. V. & Yulin, A. V. (2005). Theory of generation of new frequencies by mixing of solitons and dispersive waves in optical fibers. *Physical Review E* Vol. 72, No. 1, pp. 016619-1:10.

Stolen, R. H. & Leibolt, W. N. (1976). Optical fiber modes using stimulated four photon mixing. *Applied Optics* Vol. 15, No. 1, pp. 239-243.

Taira, K. & Kikuchi, K. (2001). Optical sampling system at 1.55 μm for the measurement of pulse waveform and phase employing sonogram characterization. *IEEE Photonics Technology Letters* Vol. 13, No. 5, pp. 505-507.

Treacy, E. B. (1971) Measurement and Interpretation of Dynamic Spectrograms of Picosecond Light Pulses. *Journal of Applied Physics* Vol. 42, No. 10, pp. 3848-3858.

Trebino, R. (2000). Frequency-Resolved Optical Gating: The Measurement of Ultrashort Laser Pulses. Kluwer, Boston.

Udem, Th.; Holzwarth, R. & Hänsch, T. W. (2002). Optical frequency metrology. *Nature* Vol. 416, No. 6877, pp. 233-237.

Wai, P. A.; Chen, H. H. & Lee, Y. C. (1990). Radiations by ''solitons'' at the zero group-dispersion wavelength of single-mode optical fibers. *Physical Review A* Vol. 41, No. 1, pp. 426-439.

Wang, A.; George, A. K. & Knight, J. C. (2006). Three-level neodymium fiber laser incorporating photonic bandgap fiber. *Optics Letters* Vol. 31, No. 10, pp. 1388-1390.

Weiner, A. M. (1983). Effect of group velocity mismatch on the measurement of ultrashort optical pulses via second harmonic generation. *IEEE Journal of Quantum Electronics* Vol. 19, No. 8 pp. 1276-1283.

Yu, H. C. Y.; Argyros, A.; Barton, G.; van Eijkelenborg, M. A.; Barbe, C.; Finnie, K.; Kong, L.; Ladouceur, F. & McNiven, S. (2007). Quantum dot and silica nanoparticle doped polymer optical fibers. *Optics Express* Vol. 15, No. 16, pp. 9989-9994.
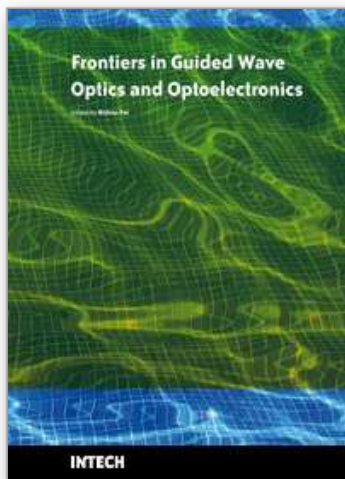
Frontiers in Guided Wave Optics and Optoelectronics

Edited by Bishnu Pal

As the editor, I feel extremely happy to present to the readers such a rich collection of chapters authored/co-authored by a large number of experts from around the world covering the broad field of guided wave optics and optoelectronics. Most of the chapters are state-of-the-art on respective topics or areas that are emerging. Several authors narrated technological challenges in a lucid manner, which was possible because of individual expertise of the authors in their own subject specialties. I have no doubt that this book will be useful to graduate students, teachers, researchers, and practicing engineers and technologists and that they would love to have it on their book shelves for ready reference at any time.

How to reference

In order to correctly reference this scholarly work, feel free to copy and paste the following:

Anatoly Efimov (2010). Time-Spectral Visualization of Fundamental Ultrafast Nonlinear-Optical Interactions in Photonic Fibers, Frontiers in Guided Wave Optics and Optoelectronics, Bishnu Pal (Ed.), ISBN: 978-953-7619-82-4, InTech, Available from: http://www.intechopen.com/books/frontiers-in-guided-wave-optics-and-optoelectronics/time-spectral-visualization-of-fundamental-ultrafast-nonlinear-optical-interactions-in-photonic-fibe

INTECH

open science | open minds